




Effect of turbulence intensity and surface tension on the emulsification process and its stationary state—A numerical study

Alexander Begemann  | Theresa Trummler  | Elias Trautner  |
Josef Hasslberger  | Markus Klein 

Institute of Applied Mathematics and Scientific Computing, Bundeswehr University, Munich, Germany

Correspondence

Theresa Trummler and Markus Klein, Institute of Applied Mathematics and Scientific Computing, Bundeswehr University, Munich, Germany.
Email: theresa.trummler@unibw.de and markus.klein@unibw.de

Funding information

Digitalization and Technology Research Center of the Bundeswehr, Grant/Award Number: MORE Project; Gauss Centre for Supercomputing e.V

Abstract

We study turbulent emulsions and the emulsification process in homogeneous isotropic turbulence (HIT) using direct numerical simulations (DNS) in combination with the volume of fluid method (VOF). For generating a turbulent flow field, we employ a linear forcing approach augmented by a proportional-integral-derivative (PID) controller, which ensures a constant turbulent kinetic energy for two phase flow scenarios and accelerates the emulsification process. For the simulations, the density ratio of dispersed and carrier phases is chosen to be similar to that of oil and water (0.9), representing a typical application. We vary the turbulence intensity and the surface tension coefficient. Thus, we modulate those parameters that directly affect the Hinze scale, which is expected to be the most stable maximum droplet diameter in emulsions in HIT. The considered configurations can be characterized with Taylor Reynolds numbers in the range of 100–140 and Weber numbers, evaluated with the velocity fluctuations and the integral length scale, of 4–70. Using the 3-D simulation results, we study the emulsification process as well as the emulsions at a statistically stationary state. For the latter, droplet size distributions are evaluated and compared. We observe a Hinze scale similarity of the size distributions considering a fixed integral length scale, that is, similar Hinze scales obtained at different turbulence intensities or for different fluid properties result in similar distributions.

KEYWORDS

direct numerical simulation (DNS), emulsification, emulsion, homogeneous isotropic turbulence (HIT)

Abbreviations: CFD, computational fluid dynamics; CFL, Courant–Friedrichs–Lewy; CSF, continuous-surface-force; DNS, direct numerical simulations; GWDI, gasoline–water direct injection; HIT, homogeneous isotropic turbulence; LBM, Lattice-Boltzmann methods; LES, Large-Eddy Simulation; PARIS, parallel robust interface simulator; PID, proportional-integral-derivative; QUICK, quadratic upstream interpolation for convective kinematics; TKE, turbulent kinetic energy; VOF, volume of fluid.

This is an open access article under the terms of the [Creative Commons Attribution-NonCommercial-NoDerivs](https://creativecommons.org/licenses/by-nc-nd/4.0/) License, which permits use and distribution in any medium, provided the original work is properly cited, the use is non-commercial and no modifications or adaptations are made.

© 2022 The Authors. The *Canadian Journal of Chemical Engineering* published by Wiley Periodicals LLC on behalf of Canadian Society for Chemical Engineering.

1 | INTRODUCTION

Emulsions are suspensions of immiscible liquids, such as oil and water, where the dispersed liquid is present in the form of poly-disperse droplets in the carrier liquid. Emulsions play an essential role in various industrial processes, such as food processing,^[1–3] oil production^[4,5] or pharmaceutical processes.^[6] Recent research is exploring the application of fuel–water emulsions for more efficient and environmentally friendly power generation. An example is gasoline–water direct injection (GWDI) for future gasoline engines,^[7,8] which can be realized by injection of gasoline–water emulsions. Other examples are fuel–water emulsions for small gas turbines^[9] or diesel engines.^[10] For these applications, a better understanding of the emulsification process and emulsions is important. One way to gain a deeper insight into the underlying mechanisms is by conducting numerical flow simulations using computational fluid dynamics (CFD). To facilitate simulations of emulsions, we propose an extension of the linear forcing^[11] to generate emulsions within a short time while ensuring its applicability to two-phase flow problems. Thus, the presented study could be a central step to make CFD simulations of emulsions feasible for industrial applications, potentially easing the design process of future gasoline engines. Further, we have applied our approach to numerically investigate emulsions of fluids with a density ratio resembling that of oil and water.

The formation of an emulsion, that is, the emulsification, requires energy input in the form of kinetic energy that results in the deformation, breakup, and coalescence of droplets. Higher turbulent kinetic energy (TKE) results in smaller droplets and vice versa. Hinze^[12] proposed that droplets break up when the droplet Weber number We_d

$$We_d = \frac{\rho_c \langle (\delta u_d)^2 \rangle d}{\sigma} \quad (1)$$

exceeds a critical value. $We_{d,crit} \cdot \rho_c \cdot \delta u_d \cdot \langle \cdot \rangle$, d , and σ denote the density of the carrier fluid, the velocity difference across the droplet (spatial averaged), the droplet diameter, and the surface tension coefficient, respectively. Using Kolmogorov theory for velocity differences^[13] ($\langle (\delta u_d)^2 \rangle \approx \varepsilon^{2/3} d^{2/3}$), the most stable droplet diameter, termed the Hinze scale, is given by

$$d_H = (We_{d,crit}/2)^{3/5} (\rho_c/\sigma)^{-3/5} \varepsilon^{-2/5}. \quad (2)$$

Thus, d_H is characterized by the ratio of the density of the carrier fluid to the surface tension coefficient ρ_c/σ and the dissipation rate ε , the latter being associated with the turbulence intensity. Note that Equation (2) has been derived for the assumption of homogeneous isotropic

turbulence (HIT) and dilute emulsions since coalescence is neglected. By fitting with experimental data, Hinze^[12] suggested $We_{d,crit} \approx 1.17$. This value has been found valid in numerical^[14] and experimental studies^[15] of dilute emulsions and has also been used for numerical studies of dense emulsions.^[16,17] In addition to this, the Hinze correlation (Equation (2)) has been studied for other multiphase configurations such as air bubbles in breaking waves,^[18,19] where Deane and Stokes^[19] found $We_{d,crit} = 4.7$, or for droplets produced in atomization processes.^[20–22]

Emulsions feature a poly-disperse droplet distribution; hence, a fundamental characteristic is the droplet size distribution. Experimental studies in stirred vessels^[23] and a Taylor-Couette flow^[15] reported a log-normal distribution considering dilute emulsions, which was also observed in the numerical study by Perlekar et al.^[14] On the other hand, for the size distributions of air bubbles in breaking waves, power laws have been proposed. For $d > d_H$, turbulent fragmentation dominates and Garrett et al.^[18] found that the distribution follows a $d^{-10/3}$ power law. Within the dynamic break-up processes, bubbles break up, and produce smaller bubbles of different sizes, including bubbles in the sub-Hinze range.^[24] For $d < d_H$, turbulent fragmentation declines and thus a less steep distribution can be expected. By fitting experimental data, Deane and Stokes^[19] proposed a $d^{-3/2}$ power law in this region. Recent numerical studies^[16,17,25] adopted these power laws for emulsions and observed a good agreement for dense emulsions, especially for $d < d_H$. Although a lot of studies have already investigated droplet size distributions, certain aspects are still not yet clarified.

Due to the relevance of emulsions for process engineering, several experimental studies have focused on different aspects. For example, Tcholakova et al.^[26,27] and Vankova et al.^[28,29] conducted comprehensive studies of the effect of various fluid properties on mean droplet sizes. Pacek et al.^[23,30] studied droplet size distributions in stirred vessels and, more recently, Yi et al.^[15] in a Taylor-Couette shear flow system. However, the limited optical accessibility of experiments in general, as well as the inherent opacity of emulsions with small droplets, imposes challenges for experimental studies and requires sophisticated measurement techniques.^[31] Another aspect is that anisotropy is usually present in experimental configurations, which means that theories derived for isotropic flows often cannot be directly applied.

Numerical simulations of multiphase flows provide time-resolved, three-dimensional data allowing for detailed studies of the complex interactions between turbulence and the dynamics of the dispersed phase. Further, fluid properties and characteristic quantities can be specifically tuned in simulations, thus enabling a precise investigation of relevant setups. For these reasons, simulations have been established to complement experimental

studies. A comprehensive review of direct numerical simulations (DNS) of droplet and bubble-laden turbulent flows can be found in Elghobashi.^[32] Emulsions, that is, liquid-liquid suspensions with a poly-disperse droplet distribution, were traditionally studied using Lattice-Boltzmann methods (LBM) and spectral forcing. Perlekar et al.^[14] investigated the droplet size distribution in HIT with a pseudo-potential LBM. Skartlien et al.^[25] simulated a surfactant-laden emulsion under weak turbulence using a free-energy LBM and Mukherjee et al.^[16] studied emulsions in HIT using an improved pseudo-potential LBM. They evaluated droplet size distributions for varying volume fractions and turbulence intensities. Further, they showed that emulsions evolve into a quasi-equilibrium cycle of coalescence and breakup-dominated processes. Recently a finite-volume approach has been employed to study emulsions. Using the volume of fluid method (VOF), Cialesi-Esposito et al.^[17] studied the effect of variations in the viscosity ratio, the volume fraction, and the surface tension on size distributions and the energy transport between different scales. The emulsification process, that is, the breakup of a liquid structure in HIT, was also the focus of various numerical investigations, such as, for example, Komrakova et al.^[33], Komrakova,^[34] Zhong and Komrakova^[35] using a free-energy LBM.

Numerical studies of emulsions usually consider emulsions under HIT, and therefore employ spectral forcing approaches, see for example, works of.^[14,16,17,33-35] As an alternative to spectral forcing, Lundgren^[11] proposed a linear forcing, which has been extended for variable length scales and non-cubic domains by Klein et al.^[36] Compared to spectral methods, the linear forcing is less computationally expensive but leads to strong oscillations resulting in longer simulation times to reach a statistically stationary state. To reduce the oscillatory nature, Carroll and Blanquart^[37] proposed a slight modification of the forcing term. Shao et al.^[38] successfully employed the originally proposed linear forcing^[11] to simulate a droplet breakup.

In this paper, we study emulsions that resemble an oil-in-water emulsion in terms of density ratio ($\rho_d/\rho_c = 0.9$). Therewith, we extend previous numerical studies by considering emulsions of fluids with matching densities.^[14,16,17] We vary the turbulence intensity, which affects the dissipation rate ε , and the surface tension coefficient σ , and thus focus on the parameters altering the Hinze scale (see Equation 2). We consider a void fraction of the dispersed phase of 12.5% and the kinematic viscosity of both phases is set to $\nu = \nu_c = \nu_d = 0.001 \text{ m}^2/\text{s}$. The scope of this work is the emulsification process and the characterization of emulsions at statistically stationary state. For the latter, we evaluate droplet size distributions. For our studies, we use DNS with the finite volume approach and the VOF method. To generate the turbulent flow field, we employ a linear forcing^[11] augmented

with a proportional-integral-derivative (PID) controller to ensure a constant TKE and to accelerate the emulsification process. The linear forcing approach has been derived for single phase flows and therefore does not account for surface tension contributions that draw or generate TKE at breakup or coalescence.^[39] Hence, here we also investigate the applicability of the linear forcing approach to multiphase flows, with a particular focus on the emulsification process, where breakup dominates and draws TKE. For comparison with theories derived for homogeneous isotropy, we follow previous studies^[14,16,17] and consider the general configuration of a HIT in a periodic box of length $L = 2\pi$.

The paper is structured as follows. In Section 2, we describe the computational method. Then, Section 3 presents the considered configurations and the numerical setup. The results part, Section 4, first studies the emulsification process and then the obtained emulsions at a statistically stationary state. Section 5 summarizes the paper.

2 | COMPUTATIONAL METHOD

All simulations for this DNS study have been performed with the state-of-the-art open source code ‘PARALLEL ROBUST INTERFACE SIMULATOR’ (PARIS).^[40] PARIS is specifically designed for simulations of multiphase flows and is widely used for DNS and LES studies of atomization processes^[36,41-45] as well as other multiphase flow configurations.^[46]

The governing equations and numerical methods are provided in Section 2.1. The implemented turbulence forcing approach is explained in Section 2.2.

2.1 | Governing equations and numerical framework

The solver uses the one-fluid formulation^[47] of the incompressible Navier-Stokes equations. The continuity and momentum equations are given as

$$\frac{\partial u_i}{\partial x_i} = 0. \quad (3)$$

$$\rho \left(\frac{\partial u_i}{\partial t} + \frac{\partial u_i u_j}{\partial x_j} \right) = -\frac{\partial p}{\partial x_i} + \frac{\partial}{\partial x_j} \left[\mu \left(\frac{\partial u_i}{\partial x_j} + \frac{\partial u_j}{\partial x_i} \right) \right] + \sigma n_i \kappa \delta_s \quad (4)$$

with the density ρ , the dynamic viscosity μ , the i th velocity component u_i , and the pressure p . In each cell, the density and viscosity values are linearly interpolated

using the local volume fraction α of the dispersed phase, which is tracked with the geometrical VOF method^[48]:

$$\rho = \alpha\rho_d + (1 - \alpha)\rho_c, \quad \mu = \alpha\mu_d + (1 - \alpha)\mu_c. \quad (5)$$

The subscripts d and c denote the dispersed and the carrier phase, respectively.

The continuous-surface-force (CSF) approach^[49] determines the surface tension force from the surface tension coefficient σ , the interface normal $n_i = \frac{\partial\alpha}{\partial x_i} / |\nabla\alpha|$, the interface indicator function $\delta_S = |\nabla\alpha|$, and the interface curvature $\kappa = \frac{\partial n_i}{\partial x_i}$. The latter is accurately computed using a state-of-the-art height function approach.^[50] For details on its implementation in PARIS, the reader is referred to the work of Aniszewski et al.^[40]

The advection of the VOF marker function is performed using a geometrical interface reconstruction algorithm. The respective transport equation is given as

$$\frac{\partial\alpha}{\partial t} + u_i \frac{\partial\alpha}{\partial x_i} = 0, \quad \alpha = \begin{cases} 1, & \text{if } \mathbf{x} \text{ is in dispersed phase.} \\ 0, & \text{if } \mathbf{x} \text{ is in carrier phase.} \end{cases} \quad (6)$$

A red-black Gauss–Seidel solver with overrelaxation is employed to solve the Poisson equation for pressure in the framework of the projection method. The simulation is advanced in time using a second-order predictor–corrector method. For the spatial discretization, the finite-volume approach is realized using a cubic grid. The velocity components are stored on a staggered grid, while the pressure and the VOF marker function, as well as the local densities and the viscosities resulting from the latter, are computed at the cell centres. The third-order ‘quadratic upstream interpolation for convective kinematics’ (QUICK) scheme has been chosen to discretize the convective term of the momentum equation, while its viscous term is treated using central differences.

2.2 | Linear forcing augmented with a PID controller

To generate HIT, a modification of the linear Lundgren forcing is employed, where the modification is motivated by the approach proposed by Carroll and Blanquart.^[37] Lundgren^[11] suggested a physical space forcing method introducing a pseudo shear term $A_F u_i$. Thus, the linearly forced momentum equations (Equation 4) of a single phase flow read as

$$\rho \left(\frac{\partial u_i}{\partial t} + \frac{\partial u_i u_j}{\partial x_j} \right) = - \frac{\partial p}{\partial x_i} + \frac{\partial}{\partial x_j} \left[\mu \left(\frac{\partial u_i}{\partial x_j} + \frac{\partial u_j}{\partial x_i} \right) \right] + A_F u_i, \quad (7)$$

where A_F denotes the forcing parameter, which controls the energy injected. Note that in this linear forcing approach, energy is injected over all scales. Assuming incompressibility and homogeneity, the TKE equation derived from Equation (7) reads as^[37]

$$\frac{dk}{dt} = -\varepsilon + 2 A_F k, \quad (8)$$

where k denotes the TKE $k = \langle \frac{1}{2} u_i' u_i' \rangle$ and ε the dissipation rate $\varepsilon = \langle \nu \frac{\partial u_i'}{\partial x_j} \frac{\partial u_i'}{\partial x_j} \rangle$ with the kinematic viscosity $\nu \cdot \langle \cdot \rangle$ indicates spatial averaging. At a statistically stationary state, Equation (8) simplifies to

$$0 = -\varepsilon_0 + 2 A_F k_0, \quad (9)$$

where the subscript 0 refers to statistical stationarity. Equation (9) gives $A_F = \frac{\varepsilon_0}{2 k_0}$ and thus A_F is the inverse of two eddy-turn over times $\tau = k/\varepsilon$. k , and ε are linked to each other and determine the integral length scale l

$$l = \frac{(u'^2)^{3/2}}{\varepsilon} \quad (10)$$

with the velocity fluctuations u' . For isotropic turbulence, these are given by

$$k = \frac{3}{2} u'^2. \quad (11)$$

Rosales and Meneveau^[51] found that such a linear forcing approach results in a turbulent flow field characterized by an integral length scale of approximately 20% of the domain size

$$l \approx 0.2 L. \quad (12)$$

Using Equations (9)–(12), the forcing parameter A_F for a desired k_0 and a chosen domain size L can be evaluated.

This linear forcing approach leads to high oscillations of turbulence metrics, such as k , and long simulation times to reach the target value k_0 . For a faster convergence towards k_0 , Carroll and Blanquart^[37] proposed to modify the magnitude of the forcing parameter A_F depending on the current ratio of k_0/k

$$A_F^{\text{Carroll}} = \frac{k_0}{k} A_F. \quad (13)$$

Alternatively to Carroll and Blanquart,^[37] we modify the forcing parameter using a PID controller

$$A_F^{\text{PID}} = \beta^{\text{PID}} A_F \quad (14)$$

where the factor β^{PID} is composed of the proportional (P), integral (I), and differential parts (D)

$$\beta^{\text{PID}} = \beta_P + \beta_I + \beta_D, \quad (15)$$

which are determined by the current normalized deviation from k_0 : $\delta_k = \frac{k(t) - k_0}{k_0}$. Consequently, β^{PID} reads as

$$\beta^{\text{PID}} = c_P \delta_k + c_I \int_0^t \delta_k(\tau) d\tau + c_D \frac{d\delta_k}{dt} \quad (16)$$

with the constants c_i for the corresponding parts P, I, and D. In this work, we used $c_P = 1$, $c_I = 1/1000$, and $c_D = 1$. In the Appendix A, we compare the temporal evolution of turbulence metrics of our forcing approach with that by Carroll and Blanquart.^[37] The enhancement of volume forcing by using controllers is also reported in the recent literature^[41,52] for different applications.

We apply our forcing to multiphase configurations with the additional surface tension force term in the momentum equation. Thus, in our case, the forced momentum equations read

$$\rho \left(\frac{\partial u_i}{\partial t} + \frac{\partial u_i u_j}{\partial x_j} \right) = - \frac{\partial p}{\partial x_i} + \frac{\partial}{\partial x_j} \left[\mu \left(\frac{\partial u_i}{\partial x_j} + \frac{\partial u_j}{\partial x_i} \right) \right] + \sigma n_i \kappa \delta_s + A_F u_i \quad (17)$$

and the TKE equation is^[39]

$$\frac{dk}{dt} = -\varepsilon + 2 A_F k + \Psi_\sigma, \quad (18)$$

where Ψ_σ denotes the surface tension contribution defined as^[39]

$$\Psi_\sigma = \frac{-\sigma}{V_d \rho_d} \frac{\partial A}{\partial t}, \quad (19)$$

with V_d and ρ_d denoting the volume and the density of the dispersed phase respectively, and A the interface area. At a stationary state of emulsions, it can be expected that breakup and coalescence processes compensate each other more or less and that, therefore, the net contribution of the surface tension term in Equation (18) is approximately zero. However, during the emulsification, interface deformation, and breakup dominate, which acts as a sink for TKE. To this end, we evaluate the magnitude of the surface tension term and

estimate advantages of a forcing approach that considers this term, see Section 4.1.

3 | CONSIDERED CONFIGURATIONS AND NUMERICAL SETUP

Our cases are characterized by a variety of parameters, the first one being the Hinze scale d_H (Equation 2). Following Hinze,^[12] we assume $We_{d,crit} \approx 1.17$, resulting in

$$d_H = 0.725 (\rho_c / \sigma)^{-3/5} \varepsilon^{-2/5}. \quad (20)$$

Recent numerical studies^[16,17] also employed this value for $We_{d,crit}$.

Further, we consider the turbulent Reynolds number

$$Re_l = \frac{lu'}{\nu}, \quad (21)$$

here evaluated with the integral length scale Equation (10) as characteristic length scale. Using Equations (2), (10), and (21), the following correlation can be obtained.^[15]

$$d_H/l \propto Re_l^{-6/5}. \quad (22)$$

Additionally, we also consider its Taylor micro-scale counterpart

$$Re_\lambda = \frac{\lambda u'}{\nu}, \quad (23)$$

with the Taylor micro-scale being $\lambda = \sqrt{15\nu/\varepsilon u'}$.

The effect of surface tension is taken into account by the Weber number We_l

$$We_l = \frac{\rho_c u'^2 l}{\sigma}, \quad (24)$$

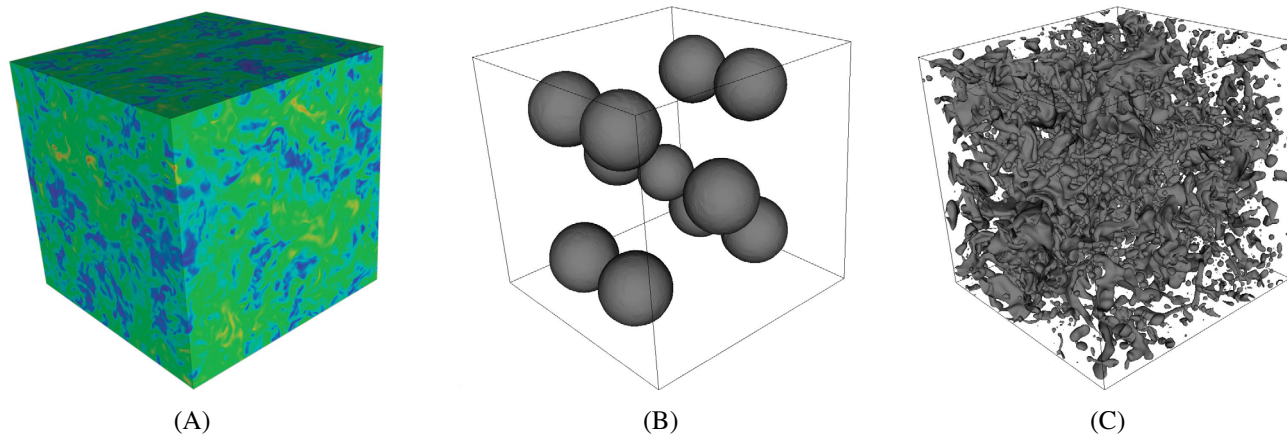
evaluated with the integral length scale l as characteristic length scale. Using Equations (2), (10), and (21), the following correlation is obtained

$$d_H/l \propto We_l^{-3/5}. \quad (25)$$

As reference time scale, we use the eddy turn-over time $\tau = k/\varepsilon$. In order to have a constant τ , we assume $\tau = \tau_0$, evaluated with k_0 and ε_0 from statistically

TABLE 1 Considered configurations, for definitions see text

Case	σ (N/m)	k_0 (m ² /s ²)	ε_0 (m ² /s ³)	τ_0 (s)	d_H/L (%)	Re_λ	Re_λ	We_1
Baseline	$2 \cdot 10^{-2}$	0.5	0.153	3.27	2.33	726	104	21
Low σ	$6 \cdot 10^{-3}$	0.5	0.153	3.27	1.14	726	104	70
High σ	$1 \cdot 10^{-1}$	0.5	0.153	3.27	6.14	726	104	4
High k	$2 \cdot 10^{-2}$	1.5	0.265	1.89	1.21	1257	137	63


FIGURE 1 Simulation setup. (A) Single-phase forcing, flow field visualized by the velocity magnitude, (B) initialization droplets with diameter $d_0 \approx 0.14 L$ (the droplet in the centre has a smaller diameter to obtain the intended volume fraction), and (C) turbulent emulsion at a statistically stationary state

stationary state. The interface area of the dispersed phase A is numerically approximated with the volume integral of the gradient of the VOF marker function $|\nabla\alpha|$. As reference for the interface area, we take the theoretically completely segregated state with $A_\infty = L^2$.

Table 1 lists the considered configurations. In our study, we vary the two parameters σ and k (directly related with the turbulence intensity and affecting ε), which both alter the Hinze scale d_H (see Equation 2). We have defined a baseline case (Baseline) and then varied the surface tension coefficient for the cases low σ and high σ . Moreover, we have increased the turbulent kinetic energy for the case high k . Note that for low σ and high k , We_1 is similar and d_H nearly identical. For all configurations, we consider a carrier fluid (c) and dispersed fluid (d) with a density ratio of $\rho_d/\rho_c = 0.9$ with $\rho_c = 1 \text{ kg/m}^3$. The kinematic viscosities are set to $\nu_d = \nu_c = 0.001 \text{ m}^2/\text{s}$. Further, for all cases, the volume fraction of the dispersed phase is set to $\alpha = 12.5\%$. The domain is a cubic box with a length of $L = 2\pi$ and periodic boundary conditions in each direction. The grid resolution has been chosen to fulfill the criterion $K_{max}\eta \geq 1.5$, see, for example, Pope.^[53] K_{max} refers to the maximum wavenumber $K_{max} = N\pi/L$, where N denotes the number of cells and L the domain length.

η refers to the Kolmogorov scale $\eta = (\nu^3/\varepsilon)^{1/4}$. For the cases with $Re_\lambda = 104$, we use $N = 384$ cells in each direction ($\approx 57e6$ cells in total), and for $Re_\lambda = 137$, we use $N = 512$ ($\approx 134e6$ cells in total). A grid study is provided in Appendix A.

The time step in the simulations is governed by the Courant–Friedrichs–Lewy number (CFL number), which is set to $CFL = 0.2$. The average time step was about $\Delta t = 8 \cdot 10^{-4} \text{ s}$ for the cases with $k = 0.5 \text{ m}^2/\text{s}^2$, and about $\Delta t = 5 \cdot 10^{-4} \text{ s}$ for the high k case ($k = 1.5 \text{ m}^2/\text{s}^2$).

The simulations are conducted as visualized in Figure 1. First, we perform single phase simulations to obtain a fully developed single-phase HIT. Therefore, the initial flow field is obtained from a Taylor–Green vortex,^[54] which is an established generic configuration for numerical studies.^[55,56] It should be noted that this starting condition is an arbitrary choice and does not affect the flow field at a statistically stationary state. It is only prescribed because the forcing requires a non-zero starting condition. Then, we initialize the dispersed phase as spherical droplets with $d_0 \approx 0.14 L$ and a smaller droplet in the centre to obtain the intended volume fraction, see Figure 1B. This approach results in a significant reduction in emulsification time and thus computational cost. Crialessi-Esposito et al.^[17] have recently employed

the same approach, and it has been found that the initial distribution has no effect on the final droplet size distribution.^[16,17]

4 | RESULTS

First, the emulsification process is analyzed in Section 4.1. In this subsection, also, the suitability of the employed linear forcing for multiphase flows is demonstrated. Then, in Section 4.2, the emulsions at a statistically stationary state are studied by means of visual inspection and droplet size distributions.

4.1 | Emulsification

In this subsection, we first analyze the temporal evolution of the interface area, representing the progress of the emulsification. Then, we study the temporal evolution of the parameters characterizing turbulence and evaluate the magnitude of the surface tension term during the emulsification. At the end of this subsection, the emulsification process of the different configurations is visualized and compared.

As described above, we initialize droplets of the dispersed phase in a fully developed single-phase HIT and, within several τ , a turbulent emulsion is obtained. Figure 2A shows the temporal evolution of the normalized interface area A/A_∞ , which reaches a statistically stationary state within about 4τ . Comparing the evolution of high k with the other cases proves that τ is the dominant time scale for the emulsification process. For high k , τ is about half of that in the other configurations (see Table 1), and the temporal evolution scaled by τ is nearly identical. Figure 2B plots the change of the interface area during the emulsification $(A - A_{\text{init}})$ normalized by the total change upon reaching a stationary state $(A_0 - A_{\text{init}})$, where A_{init} refers to the initial interface area and A_0 to the interface area at statistically stationary state. This visualization demonstrates that the slope of the normalized change of the interface area is nearly the same for all configurations. Further, the d_H similarity can already be seen in the similar interface areas obtained for high k and low σ .

Figure 3 depicts the temporal evolution of the TKE k , the dissipation rate ε , and the integral length scale l evaluated for the two phase flow. Due to our forcing approach with the PID controller, k immediately reaches the target value, see Figure 3A. The dissipation rate slightly underestimates the expected value (Figure 3B), and thus the integral length scale is slightly higher than the expected value of approximately 20% in linearly

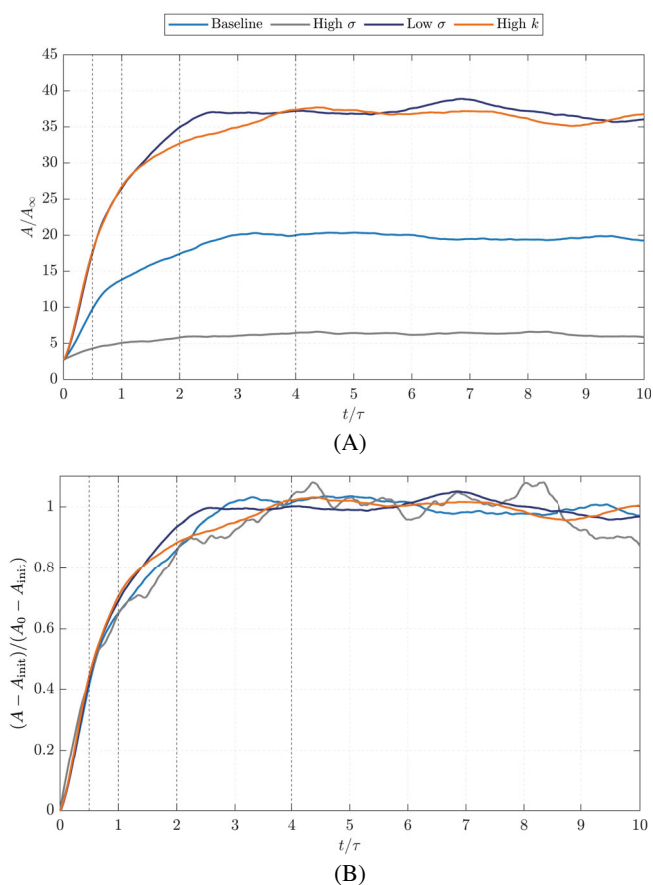


FIGURE 2 (A) Temporal evolution of the normalized interface area A/A_∞ for the different cases normalized by the eddy turn-over time τ . (B) $(A - A_{\text{init}})/(A_0 - A_{\text{init}})$ over t/τ for the different cases, A_{init} and A_0 refer to the initial interface area and the interface area at stationary state, respectively. Dashed vertical lines indicate the time instants visualized in Figure 5

forced turbulence^[51] (Figure 3C). The overall good agreement with earlier results in the literature^[37,51] proves the suitability of linear forcing for multiphase flows in general and that of the proposed extension with the PID controller in particular.

Figure 4 plots the temporal evolution of the surface tension term $\Psi_\sigma = \frac{-\sigma}{V_d \rho_d} \frac{\partial A}{\partial t}$, which is not directly considered by the linear forcing, see also Section 2.2. As expected, there is only a contribution during the emulsification process, where the droplet breakup acts as a sink for the TKE ($\Psi_\sigma < 0$). For decreasing σ , $|\Psi_\sigma|$ increases. This indicates a significantly higher $\frac{\partial A}{\partial t}$, and thus breakup rate, which even compensates the effect of the smaller σ on Ψ_σ . For configurations with a lower σ , the breakup of droplets requires less energy and thus occurs more frequently. Consequently, with a lower σ , more TKE is drawn, resulting in a higher TKE input by the forcing, which then amplifies further breakup. This process continues until a statistically stationary state is reached.

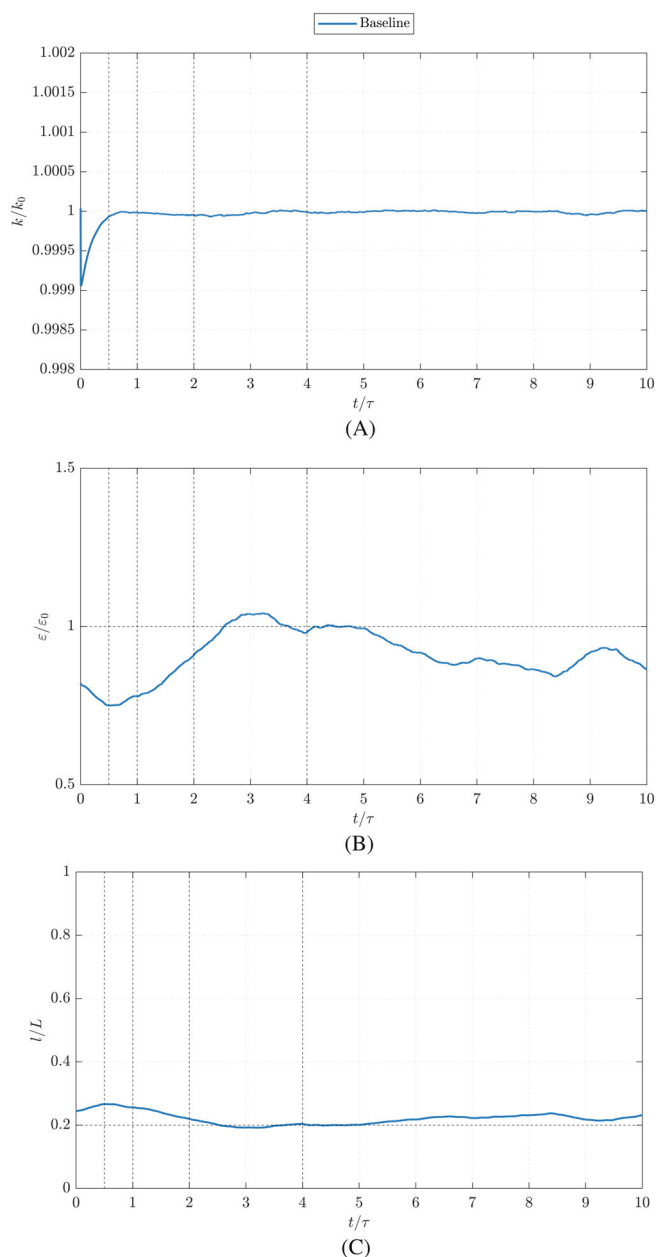


FIGURE 3 Temporal evolution of (A) turbulent kinetic energy k/k_0 , (B) dissipation rate $\varepsilon/\varepsilon_0$, and (C) integral length scale l/L for the baseline case. Dashed vertical lines indicate the time instants visualized in Figure 5

Comparing the evolution of the surface term (Figure 4) for the cases high/low σ reveals that the low σ case reaches the statistically stationary state later. This can be explained by the fact that the surface tension term requires more energy for low σ . Thus, a forcing method, where the Ψ_σ is directly fed back, would lead to a higher energy input during the emulsification, accelerating this process. At a statistically stationary state ($t > 4\tau$), the breakup process and coalescence compensate each other, thus letting the net contribution of Ψ_σ vanish.

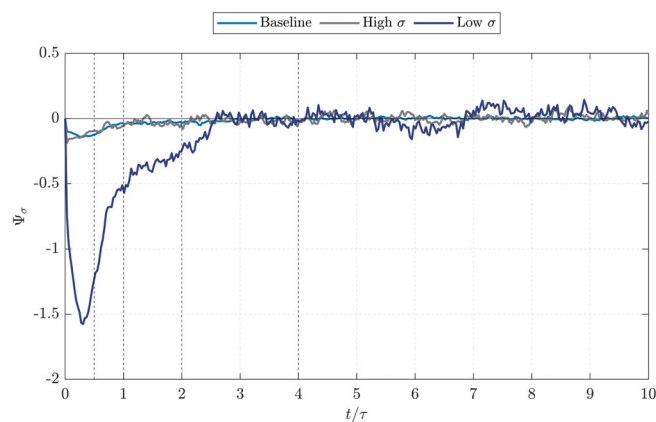


FIGURE 4 Temporal evolution of the surface tension term Ψ_σ for varying surface tension coefficients σ . Dashed vertical lines indicate the time instants visualized in Figure 5

Figure 5 illustrates the emulsification process for the different configurations at $t/\tau = 0.5$ (i), $t/\tau = 1$ (ii), $t/\tau = 2$ (iii), and $t/\tau = 5$ (iv). These time steps were chosen because most of the emulsification takes place within the first two eddy turn-over times. Already at $t/\tau = 0.5$, the initialized droplets are significantly deformed. Note that some structures appear truncated by the periodic boundary condition in each direction, and thus smaller structures, which are cut-off, are visible at the boundaries. As expected, with decreasing σ or higher TKE, the interfaces become more deformed and wrinkled. With increasing time, the dispersed structures are increasingly deformed and break up into smaller structures. Between $t/\tau = 2$ and $t = 4\tau$, the visual impression does not change much. At $t = 4\tau$ (Figure 5A–D,iv), all configurations have reached a statistically stationary state. The subsequent subsection examines this state in detail and compares the droplet size distributions.

4.2 | Characterization of turbulent emulsions at stationary state

In this subsection, we first analyze and compare the emulsions obtained for the different configurations. Then, the droplet size distributions are compared and discussed.

Figure 5A–D,iv (last column) visualizes the turbulent emulsion obtained at statistically stationary state ($t = 4\tau$). As expected, with increasing We_l (decreasing d_{Hl}), the dispersed phase is present in smaller droplets. For high σ (see Figure 5A,iv), larger structures are present and the distribution of the structures is more inhomogeneous than in the other cases. Further, there is good optical accessibility, which is no longer present in the other cases. In the

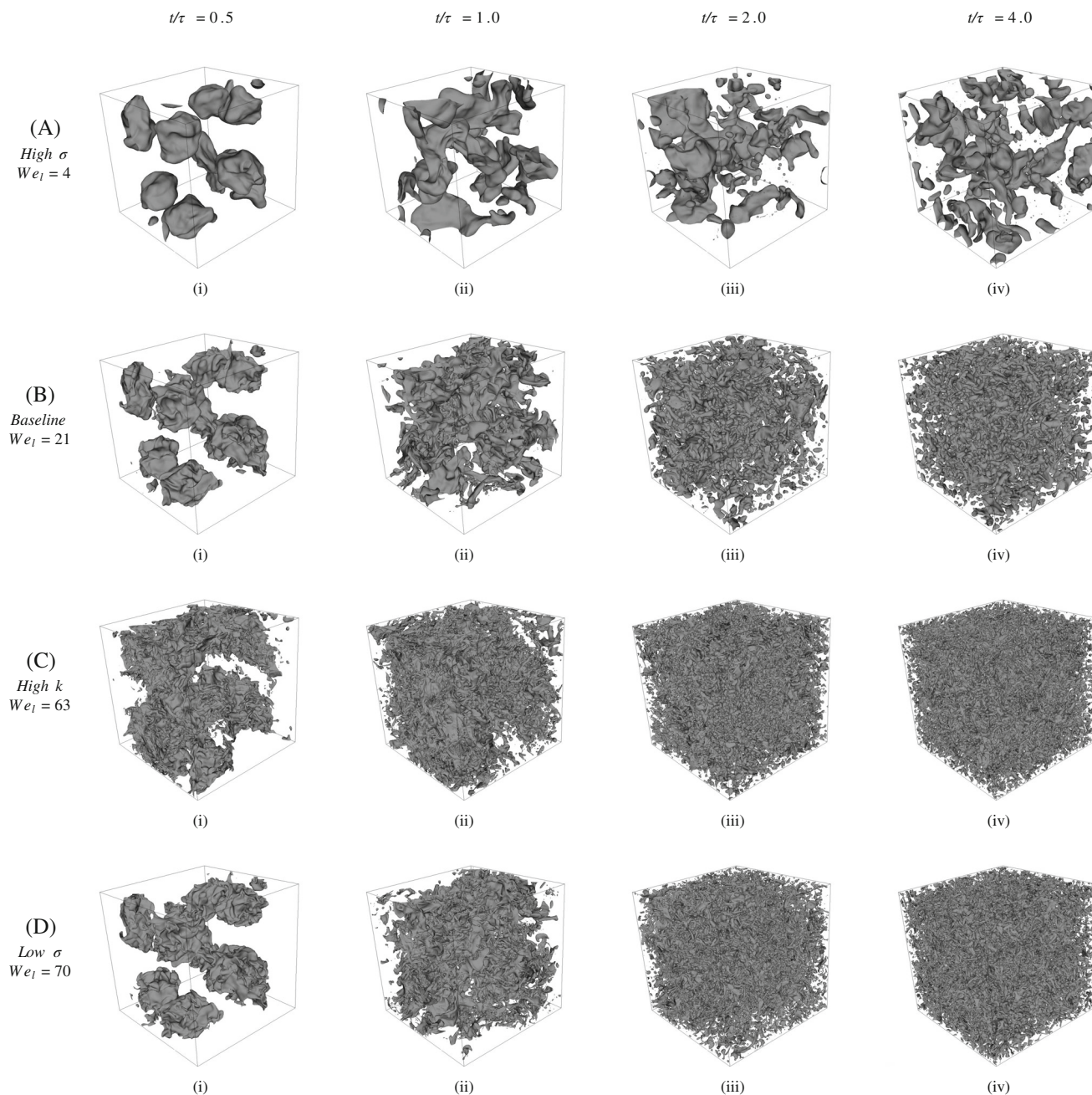


FIGURE 5 Emulsification process visualized for the different configurations. Columns correspond to different time instants and rows to different configurations. For the initialization of the dispersed phase, see Figure 1. Iso-surface $\alpha = 0.5$

Baseline case (see Figure 5B,iv), the formed droplets are already considerably smaller. This trend is resumed for the other cases (Figure 5C,D), where the droplet size decreases further with increasing We_l . The visual impression confirms a d_H/We_l similarity, compare Figure 5C,D,iv. Further, the employed Weber number We_l , evaluated with the integral length scale, appears to be a representative dimensionless number to characterize emulsions.

Figure 6 compares the probability density function (PDF) of the droplet size distributions for the different cases. The data has been sampled every eddy turn-over

time τ and is averaged for six time instants each. Droplets with an equivalent spherical diameter smaller than four cells are neglected. We chose this cut-off scale based on a variety of publications in the VOF context, for example.^[20,44,45,57] Droplets smaller than this tend to be unreliable due to numerical errors in the two-phase algorithms, for example, reconstruction and curvature computation. The observation from the time instants taken at a statistically stationary state (Figure 5A–D,iv) is reflected in the PDFs $P(d_i)$. For larger d_H and smaller We_l , the distribution is more shifted towards larger droplet sizes. For

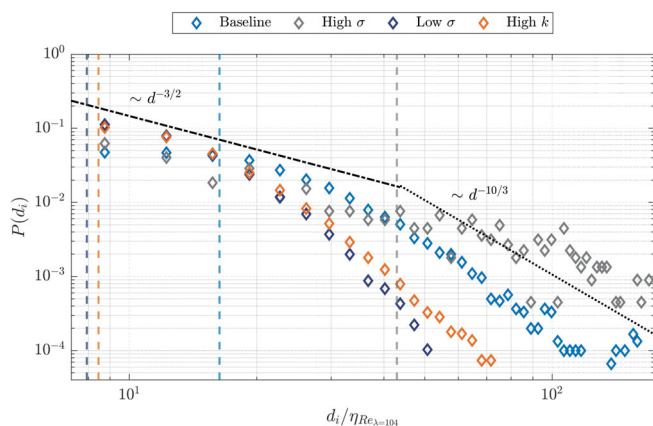


FIGURE 6 Droplet size distribution for the different cases. The data have been sampled every eddy turn-over time τ and are averaged for six time instants each after reaching the statistically stationary state. The dashed vertical lines indicated the Hinze scale d_H , where the colour corresponds to the respective case

similar d_H , for example, similar We_l , the droplet size distributions are very similar, as can be seen for the cases of low σ and high k . For the case of high k , the Hinze scale is somewhat larger and thus the PDF is slightly shifted to the right, especially at larger droplet sizes. For air bubbles in breaking waves, Deane and Stokes^[19] observed a $-3/2$ exponential scaling of bubbles smaller than the Hinze scale ($d < d_H$) and Garrett et al.^[18] found that the distribution of bubbles larger than Hinze ($d_H < d$) follows a $-10/3$ exponential scaling. Recent numerical studies^[16,17,25] successfully adopted these power laws for emulsions. The two scaling laws are indicated in Figure 6 and a good agreement with these scaling laws can be observed for the cases with high We_l (low σ , high k). However, for small We_l , the distributions are not as smooth and the agreement with the known scaling laws decreases. Results recently shown by Cialesi-Esposito et al.^[17] exhibit a similar trend for small We_l . A smaller We_l correlates with a larger d_H and thus a higher d_H/L ratio. If the d_H/L ratio is too high, the domain size may no longer be representative and biases the droplet size distribution. Based on our results, we conjecture that the d_H/L ratio should be $d_H/L \leq 0.02$. However, further research on this topic, also considering different sampling rates, is necessary to reach a final conclusion. Another important aspect of the size distributions and their alignment with these scaling laws is the volume fraction of the dispersed phase. For example, Cialesi-Esposito et al.^[17] reported that the $-10/3$ scaling law for larger droplets fits best when the volume fraction is below 10%, with a small loss of accuracy for values above this volume fraction.

5 | CONCLUSIONS

In this work, we numerically studied turbulent emulsions subjected to different turbulence intensities and surface tension coefficients. For this purpose, we performed DNS in a generic configuration of HIT in a periodic box. For the turbulence forcing, we employed a linear approach, where we adjusted the forcing parameter with a PID controller to ensure constant TKE.

The first part focused on the verification of the forcing method, whose applicability to multiphase flows we successfully demonstrated. To this end, we examined the surface tension term, which is not considered by the forcing. As expected, the surface tension term only plays a role during emulsification and consideration of this term in the forcing is expected to accelerate the emulsification. At a stationary state, the simultaneous breakup and coalescence processes let the net contribution of this term vanish. Regarding emulsification, the results have shown that the emulsification process scales with the eddy turn-over time.

The second part was devoted to turbulent emulsions at a statistically stationary state. We found that emulsions can be characterized by the Weber number evaluated with the integral length scale We_l . For the different cases investigated, we observed a d_H/We_l similarity for the visual impression of emulsions and the droplet size distribution, that is, for similar d_H/We_l , we obtain similar droplet size distributions and emulsions. We compared the droplet size distributions with previously proposed distribution laws and found good agreement with these laws for high We_l .

In future studies, we plan to investigate the effects of different density ratios of carrier and dispersed phase on the emulsification process and droplet size distribution. Of particular interest are also configurations where the density of the dispersed phase is higher than that of the carrier phase, similar to a water-in-gasoline emulsion relevant to GWDI. In addition, we plan to study emulsions in a more realistic configuration, such as in a channel flow.

The stability of emulsions in decaying turbulence, that is, without further energy input, also represents a central aspect and is of particular relevance for the realization of GWDI. When there is no further energy input, from a thermodynamic point of view, only energy-releasing processes, such as minimization of the surface area and reduction of the potential height of the heavier phase, are possible. Thus, emulsions segregate in decaying turbulence due to coalescence and sinking of the heavier phase. The numerical investigation of such segregation processes is the subject of our current research.

ACKNOWLEDGEMENTS

This project received funding from *dtec.bw* - Digitalization and Technology Research Center of the Bundeswehr—under the project *MORE*, which is gratefully acknowledged. Further, the authors thank the Gauss Centre for Supercomputing e.V. (www.gauss-centre.eu) for funding this project by providing computing time on the GCS Supercomputer SuperMUC-NG at the Leibniz Supercomputing Centre (www.lrz.de). Open Access funding enabled and organized by Projekt DEAL.

CONFLICT OF INTEREST

The authors declare that they have no known competing financial interests or personal relationships that could have appeared to influence the work reported in this paper.

DATA AVAILABILITY STATEMENT


The data that support the findings of this study are available from the corresponding author upon reasonable request.

ORCID

Alexander Begemann  <https://orcid.org/0000-0003-4770-5123>

Theresa Trummler  <https://orcid.org/0000-0001-8869-5860>

Elias Trautner  <https://orcid.org/0000-0002-0561-3450>

Josef Hasslberger  <https://orcid.org/0000-0003-3865-7035>

Markus Klein  <https://orcid.org/0000-0003-2637-2104>

REFERENCES

- [1] R. Walker, E. A. Decker, D. J. McClements, *Food Funct.* **2015**, 6, 41.
- [2] R. Zhang, Z. Zhang, H. Zhang, E. A. Decker, D. J. McClements, *Food Hydrocolloids* **2015**, 45, 175.
- [3] D. Guzey, D. J. McClements, *Adv. Colloid Interface Sci.* **2006**, 128, 227.
- [4] C. Dicharry, D. Arla, A. Sinquin, A. Graciaa, P. Bouriat, *J. Colloid Interface Sci.* **2006**, 297, 785.
- [5] V. Angardi, A. Etehad, Ö. Yücel, *J. Energy Resour. Technol.* **2021**, 144, 040801.
- [6] A. Spornath, A. Aserin, *Adv. Colloid Interface Sci.* **2006**, 128, 47.
- [7] F. Hoppe, M. Thewes, J. Seibel, A. Balazs, J. Scharf, *SAE International Journal of Engines* **2017**, 10, 2500.
- [8] C. Heinrich, H. Dörksen, A. Esch, K. Krämer, *International Conference on Knocking in Gasoline Engines*, Springer, Cham **2017**, p. 322.
- [9] M. Chmielewski, P. Niszczota, M. Gieras, *Energy* **2020**, 211, 118961.
- [10] S. Welscher, M. H. Moradi, A. Vacca, P. Bloch, M. Grill, U. Wagner, M. Bargende, T. Koch, *Int. J. Engine Res.* **2021**, 1, <https://doi.org/10.1177/14680874211044297>
- [11] T. S. Lundgren, *Linearly Forced Isotropic Turbulence*, Annual Research Briefs Center for Turbulence Research, Stanford, CA **2003**, p. 461.
- [12] J. O. Hinze, *AIChE J.* **1955**, 1, 289.
- [13] G. Batchelor, *Math. Proc. Cambridge Philos. Soc.* **1951**, 47, 359.
- [14] P. Perlekar, L. Biferale, M. Sbragaglia, S. Srivastava, F. Toschi, *Phys. Fluids* **2012**, 24, 065101.
- [15] L. Yi, F. Toschi, C. Sun, *J. Fluid Mech.* **2021**, 912, A13.
- [16] S. Mukherjee, A. Safdari, O. Shardt, S. Kenjeres, H. E. A. Van den Akker, *J. Fluid Mech.* **2019**, 878, 221.
- [17] M. Cialesi-Esposito, M. E. Rosti, S. Chibbaro, L. Brandt, *J. Fluid Mech.* **2022**, 940, A19.
- [18] C. Garrett, M. Li, D. Farmer, *Journal of Physical Oceanography* **2000**, 30, 2163.
- [19] G. B. Deane, M. D. Stokes, *Nature* **2002**, 418, 839.
- [20] Y. Ling, D. Fuster, G. Tryggvason, S. Zaleski, *J. Fluid Mech.* **2019**, 859, 268.
- [21] C. R. Constante-Amores, L. Kahouadji, A. Batchvarov, S. Shin, J. Chergui, D. Juric, O. K. Matar, *J. Fluid Mech.* **2021**, 922, A6.
- [22] B. Zhang, S. Popinet, Y. Ling, *Int. J. Multiphase Flow* **2020**, 130, 103362.
- [23] A. Pacek, C. Man, A. Nienow, *Chem. Eng. Sci.* **2005**, 1998, 53.
- [24] A. Rivière, W. Mostert, S. Perrard, L. Deike, *J. Fluid Mech.* **2021**, 917, A40.
- [25] R. Skartlien, E. Sollum, H. Schumann, *J. Chem. Phys.* **2013**, 139, 174901.
- [26] S. Tcholakova, N. D. Denkov, T. Danner, *Langmuir* **2004**, 20, 7444.
- [27] S. Tcholakova, N. Vankova, N. D. Denkov, T. Danner, *J. Colloid Interface Sci.* **2007**, 310, 570.
- [28] N. Vankova, S. Tcholakova, N. D. Denkov, I. B. Ivanov, V. D. Vulchev, T. Danner, *J. Colloid Interface Sci.* **2007**, 312, 363.
- [29] N. Vankova, S. Tcholakova, N. D. Denkov, V. D. Vulchev, T. Danner, *J. Colloid Interface Sci.* **2007**, 313, 612.
- [30] A. Pacek, A. Nienow, I. Moore, *Chem. Eng. Sci.* **1994**, 49, 3485.
- [31] M. Koegl, C. Mull, Y. N. Mishra, S. Will, L. Zigan, *Appl. Opt.* **2020**, 59, 1136.
- [32] S. Elghobashi, *Annu. Rev. Fluid Mech.* **2019**, 51, 217.
- [33] A. Komrakova, D. Eskin, J. J. Derksen, *AIChE J.* **2015**, 61, 2618.
- [34] A. Komrakova, *Can. J. Chem. Eng.* **2019**, 97, 2727.
- [35] C. Zhong, A. Komrakova, *Int. J. Numer. Methods Heat Fluid Flow* **2019**, 29, 2407.
- [36] M. Klein, N. Chakraborty, S. Ketterl, *Flow, Turbul. Combust.* **2017**, 99, 955.
- [37] P. L. Carroll, G. Blanquart, *Phys. Fluids* **2013**, 25, 105114.
- [38] C. Shao, K. Luo, Y. Yang, J. Fan, *Int. J. Multiphase Flow* **2018**, 107, 263.
- [39] M. S. Dodd, A. Ferrante, *J. Fluid Mech.* **2016**, 806, 356.
- [40] W. Aniszewski, T. Arrufat, M. Cialesi-Esposito, S. Dabiri, D. Fuster, Y. Ling, J. Lu, L. Malan, S. Pal, R. Scardovelli, G. Tryggvason, P. Yecko, S. Zaleski, *Comput. Phys. Commun.* **2021**, 263, 107849.
- [41] S. Ketterl, M. Klein, *Flow, Turbul. Combust.* **2018**, 101, 413.
- [42] J. Hasslberger, S. Ketterl, M. Klein, N. Chakraborty, *J. Fluid Mech.* **2019**, 859, 819.
- [43] F. J. Salvador, S. Ruiz, M. Cialesi-Esposito, I. Blanquer, *Int. J. Multiphase Flow* **2018**, 102, 49.

- [44] Y. Ling, S. Zaleski, R. Scardovelli, *Int. J. Multiphase Flow* **2015**, 76, 122.
- [45] Y. Ling, D. Fuster, S. Zaleski, G. Tryggvason, *Physical Review Fluids* **2017**, 2, 014005.
- [46] J. Hasslberger, M. Klein, N. Chakraborty, *J. Fluid Mech.* **2018**, 857, 270.
- [47] A. Prosperetti, G. Tryggvason, *Computational Methods for Multiphase Flow*, Cambridge University Press, Cambridge, UK **2007**.
- [48] C. W. Hirt, B. D. Nichols, *J. Comput. Phys.* **1981**, 39, 201.
- [49] J. U. Brackbill, D. B. Kothe, C. Zemach, *J. Comput. Phys.* **1992**, 100, 335.
- [50] S. Popinet, *J. Comput. Phys.* **2009**, 228, 5838.
- [51] C. Rosales, C. Meneveau, *Phys. Fluids* **2005**, 17, 095106.
- [52] E. Tangemann, M. Klein, *Fluids* **2020**, 5, 130.
- [53] S. B. Pope, *Turbulent flows*, Cambridge University Press, Cambridge, UK **2001**.
- [54] M. E. Brachet, D. I. Meiron, S. A. Orszag, B. Nickel, R. H. Morf, U. Frisch, *J. Fluid Mech.* **1983**, 130, 411.
- [55] J. Hasslberger, L. Engelmann, A. Kempf, M. Klein, *Phys. Fluids* **2021**, 33, 015117.
- [56] M. Reissmann, J. Hasslberger, R. D. Sandberg, M. Klein, *J. Comput. Phys.* **2021**, 424, 109859.
- [57] J. Shinjo, A. Umemura, *Int. J. Multiphase Flow* **2010**, 36, 513.

How to cite this article: A. Begemann, T. Trummler, E. Trautner, J. Hasslberger, M. Klein, *Can. J. Chem. Eng.* **2022**, 100(12), 3548. <https://doi.org/10.1002/cjce.24515>

APPENDIX A: VALIDATION FORCING

To validate our forcing approach, we simulated the $Re_\lambda = 110$ case of Carroll and Blanquart^[37] employing our forcing augmented with a PID controller. Figure A1 compares the temporal evolution of the

TKE k and the dissipation rate ε with the results by Carroll and Blanquart.^[37] As expected, the target TKE k_0 is reached faster with the PID augmented forcing and k remains at k_0 . Regarding the evolution of the dissipation rate ε , it can be seen that with the PID augmented forcing, there is no high overshoot at the beginning.

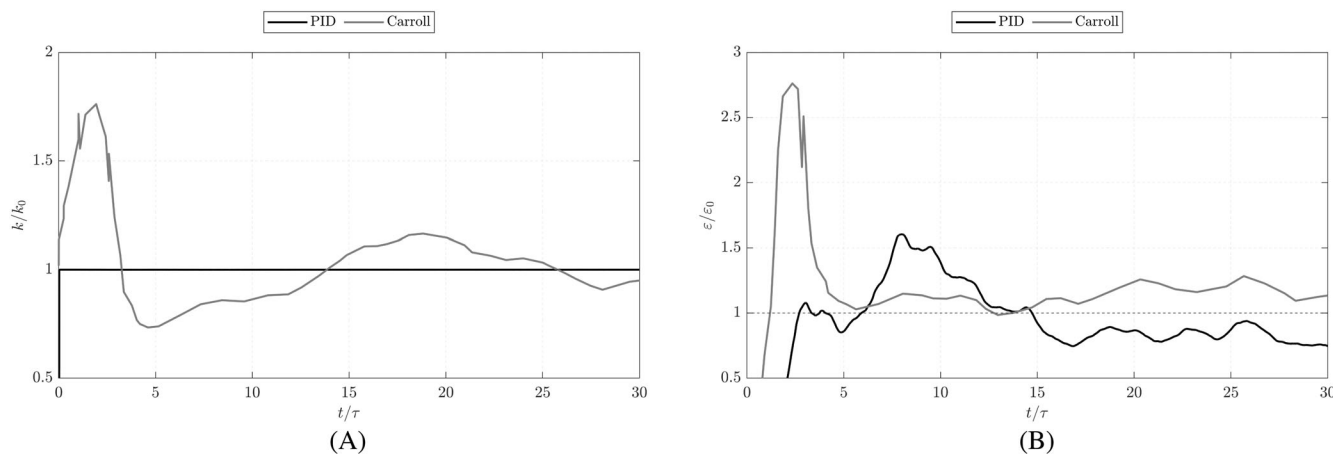


FIGURE A1 Comparison of the PID augmented forcing with the Carroll-forcing.^[37] Single phase case with $Re_\lambda = 110$. (A) Temporal evolution of normalized turbulent kinetic energy k/k_0 and (B) of normalized dissipation rate $\varepsilon/\varepsilon_0$. PID, proportional-integral-derivative

APPENDIX B: GRID STUDY

To verify that the employed grid resolution is sufficient, we conducted a grid study considering the resolutions 384^3 and 512^3 for the *Low* σ case ($Re_\lambda = 104$). Figure B1 compares the temporal evolution of the normalized interface area A/A_∞ , the normalized dissipation rate $\varepsilon/\varepsilon_0$, and the PDF of the droplet size distribution

of the droplet size distribution on the two different grid resolutions. At 384^3 and at 512^3 , the interface area and the dissipation rate at a statistically stationary state are in good agreement, indicating grid convergence. The comparison of the PDFs (Figure B1C) shows a qualitatively good agreement, especially with regard to the slopes in the ranges $d < d_H$ (sub-Hinze) and $d > d_H$.

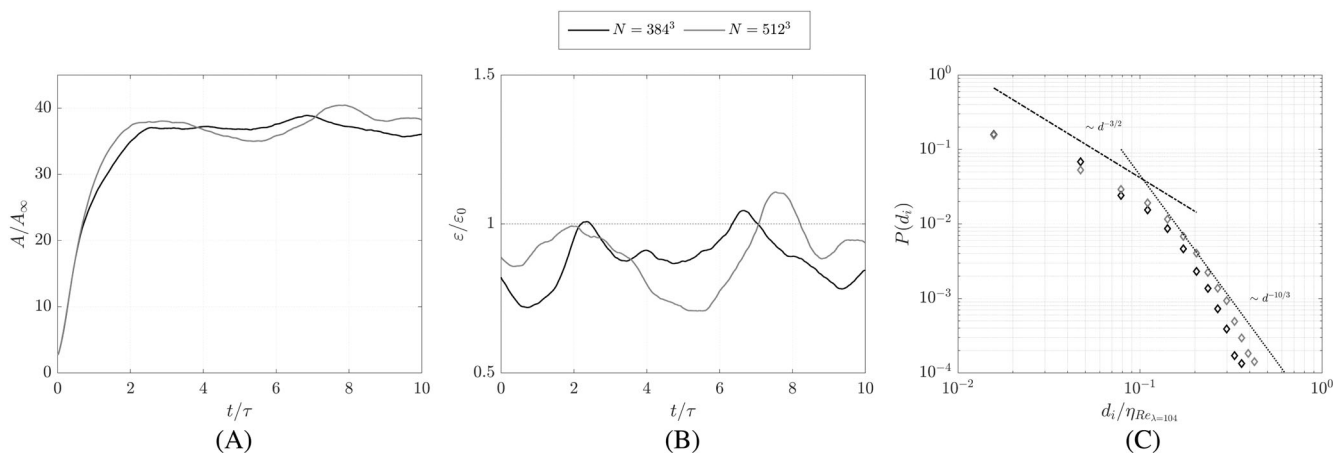


FIGURE B1 (A) Temporal evolution of the normalized interface area A/A_∞ , (B) the normalized dissipation rate $\varepsilon/\varepsilon_0$, and (C) the PDF of the droplet size distribution of the *low* σ case ($Re_\lambda = 104$) on the grid resolutions 384^3 and 512^3 . PDF, probability density function